Available online at www.sciencedirect.com
ScienceDirect
Journal of Power Sources 181 (2008) 8–16
JOURNAL OF POWER SOURCES
www.elsevier.com/locate/jpowsour

Numerical modelling of radiative heat transfer in an internal indirect reforming-type SOFC

Grzegorz Brus, Janusz S. Szmyd *

AGH-University of Science and Technology, 30-059 Krakow, Poland

Received 31 August 2007; received in revised form 9 November 2007; accepted 6 December 2007
Available online 27 December 2007

Abstract

The present paper describes numerical modelling of the radiative heat transfer process in the module chamber of an internal indirect reforming-type SOFC. The ability to do internal reforming is one of the characteristics of high-temperature fuel cells, SOFC. As in any high-temperature system, radiative heat transfer is important. In this article, heat transfer between the fuel reformer surface and all other surfaces facing the reformer surfaces is modelled. Governing equations for radiative heat transfer are described using Hottel's zone method. The resulting radiation–conduction conjugate heat transfer problems are numerically solved with a combination of Gauss–Seidel and Newton–Raphson methods. The steam reforming reaction occurring inside the fuel reformer is described using Achenbach model. The obtained results indicate that, for the development of effective indirect internal reforming, the position of the reformer in the module chamber and emissivity of the surfaces of the reformer, cell and other elements in the SOFC module all play a key role.

Keywords: Solid oxide fuel cell; Reforming system; Numerical modelling; Heat transport phenomena

1. Introduction

Due to their high efficiency and the low level of pollution they emit into the environment, solid oxide fuel cells (SOFCs) have the potential to become one of the most important energy-conversion devices. A solid oxide fuel cell consists of two porous ceramic electrodes (the cathode and anode) separated by a solid ceramic electrolyte. A typical SOFC uses solid oxides such as yttria-stabilized zirconia (YSZ) for the electrolyte [1]. It can use hydrogen, carbon monoxide, or hydrocarbons as fuel and air or oxygen as oxidants. The operation temperature of an SOFC is 700–1100 °C and operates at atmospheric or elevated pressures [2]. Hydrocarbons are the most suitable fuels for SOFCs to achieve high efficiency from natural resources [3]. For hydrocarbon-based fuel, three types of fuel conversion can be considered in reforming reactions: an external reforming system, an indirect internal reforming system and a direct internal reforming system. High-temperature SOFC eliminates the need for an expensive external reforming system. The possibility of using internal reforming is one of the characteristics of high-temperature fuel cells, SOFC. Strong endothermic fuel reforming reactions can be thermally supported by the transfer of the heat generated due to the sluggishness of electrochemical reactions, diffusion of participating chemical species and ionic and electric resistance. However, for high-temperature operation, thermal management of the SOFC system becomes an important issue. To carry out thermal management properly, detailed modelling and detailing of numerical analyses of the phenomena occurring inside the SOFC system are required.

Thermal models of fuel cells that use heat transfer correlations for assumed fluid flow configurations have been designed in the past [4]. The Suzuki group [5,6] proposed a quasi-two-dimensional model for numerical studies on the performance of a single tubular SOFC cell under practical operating conditions. Their model takes into account the air and fuel flow velocity fields, ohmic and thermodynamic heat generation, convective heat transfer, mass transfer of participating chemical species, including the electrochemical processes and the electric potential and electric current in the electrodes and electrolyte [5]. The results from this model were applied to the performance analysis of a tubular SOFC/micro-gas turbine hybrid system [6].

* Corresponding author at: AGH-University of Science and Technology, 30 Mickiewicza Avenue, 30-059 Krakow, Poland. Tel.: +48 12 6172694; fax: +48 12 6332316.
E-mail address: janusz@agh.edu.pl (J.S. Szmyd).

0378-7753/$ – see front matter © 2008 Elsevier B.V. All rights reserved.
doi:10.1016/j.jpowsour.2007.12.064

Nomenclature

A	area (m^2)
C_p	specific heat ($J\,kg^{-1}\,K^{-1}$)
d	thickness (m)
E	black-body flux density ($W\,m^{-2}$)
H_j	incident radiant flux density ($W\,m^{-2}$)
l_{ij}	distance between ith and jth elements (m)
m	molar fraction
M_j	molar mass of j component ($kg\,mol^{-1}$)
$\dot{n}$	molar flow rate ($mol\,s^{-1}$)
P	pressure (Pa)
q	heat flux (W)
R	reaction rate ($mol\,m^{-3}\,s^{-1}$)
R_u	universal gas constants, 8.314472 ($J\,mol^{-1}\,K^{-1}$)
$s_i s_j$	direct exchange area (m^2)
$S_i S_j$	total interchange area (m^2)
S_R	heat generation coming from reforming reaction ($W\,m^{-3}$)
T	temperature (K)
U	velocity ($m\,s^{-1}$)
W	radiosity ($W\,m^{-2}$)
x, y, z	axial coordinates

Greek symbols

δ	Kronecker delta
ε	emissivity
ε_0	porosity
θ	angle
λ	wavelength (m)
λ_j	thermal conductivity ($W\,m^{-1}\,K^{-1}$)
μ	dynamic viscosity (Pa s)
ρ	reflectance
ρ_0	density ($kg\,m^{-3}$)
σ	Stefan–Boltzmann constant, 5.6667×10^{-8} ($W\,m^{-2}\,K^{-4}$)
φ	view factor

Subscripts

B	bottom of geometry system
eff	effective
f	fluid
i, j	ordinals numbers
max	maximum value
o	ambient
R	reformer
sd	solid
sh	shift reaction
st	steam reforming reaction
S	side walls
T	top of geometry system

A steady-state model of an indirect internal reforming solid oxide fuel cell was developed by Aguiar et al. [2] to analyse the thermal coupling of the reforming and electrochemical reactions. In their analysis, the configuration was an annular design where the fuel call was constructed around a tubular reformer. Their model was based on a heterogeneous, two-dimensional steam reforming packed-bed reactor model coupled with a one-dimensional SOFC one. Temperature distributions in three-dimensional models of planar SOFC have been achieved by coupling the electrochemical effects with the solution of the Navier-Stokes equations of motion and energy/mass conservation [7]. As in any high-temperature system, radiative heat transfer is important. However, most existing models neglect its effects [8]. Yakabe et al. [9] found that including radiative heat exchange within the flow channels resulted in a flatter distribution of the temperature profile along the fuel cell. Murthy and Fedorov [8] demonstrated radiation heat transfer effects for accurate prediction of the temperature field and fuel cell output voltage. Damm and Fedorov [10] have recently reviewed radiative heat transfer in SOFC components and materials.

Experiments have been carried out by Achenbach and Riensche [11] to determine the kinetics of the methane/steam reforming process in/on anode materials of a solid oxide fuel cell. Their tests [11] showed that H_2O partial pressure has no catalytic effect on the reaction. They have also proposed an equation for the reforming kinetics in the form of the Arrhenius-type independence of the H_2O partial pressure and proportional to the methane (CH_4) partial pressure [11]. Their methane/steam reforming kinetics model [11] has been adopted to numerical analysis of a planar solid fuel cell stack [12] as well as to a tubular solid oxide fuel cell with accompanying indirect internal fuel reforming [6]. An alternative model of the methane reforming reaction rate was proposed by Odegard et al. [13]. This model [13] was used in numerical analyses of the characteristics of tubular SOFC with internal reformer systems by different research groups [14,15].

The present paper describes a three-dimensional numerical model of heat transfer process in the module chamber of an internal indirect reforming-type SOFC. Heat transfer between the fuel reformer surface and all other surfaces facing the reformer surface is modelled. The Achenbach model [12] is use to describe the steam reforming process occurring inside the fuel reformer and resulting radiation–conduction–convection conjugate heat transfer problems are numerically solved by the Gauss–Seidel and Newton–Raphson methods. This model can be applied for different configurations and/or characteristics of the system components.

2. The formulation and numerical scheme

The geometry of the problem to be considered is shown schematically in Fig. 1a (a detailed description on the system discussed in this paper may be found in Ref. [27]). The surfaces in the system are assumed to be grey and the gases in the SOFC chamber are assumed to be transparent. The supplied fuel to the system is the methane (CH_4). The gaseous fluids are assumed to be Newtonian and the flow of fuel inside the fuel reformer is assumed to be laminar, steady and occurring in one direction. The effect of the buoyant convection is not considered. All chemical components of working fluids in the system are considered to be the ideal gases and the temperature of in-flow fuel is taken

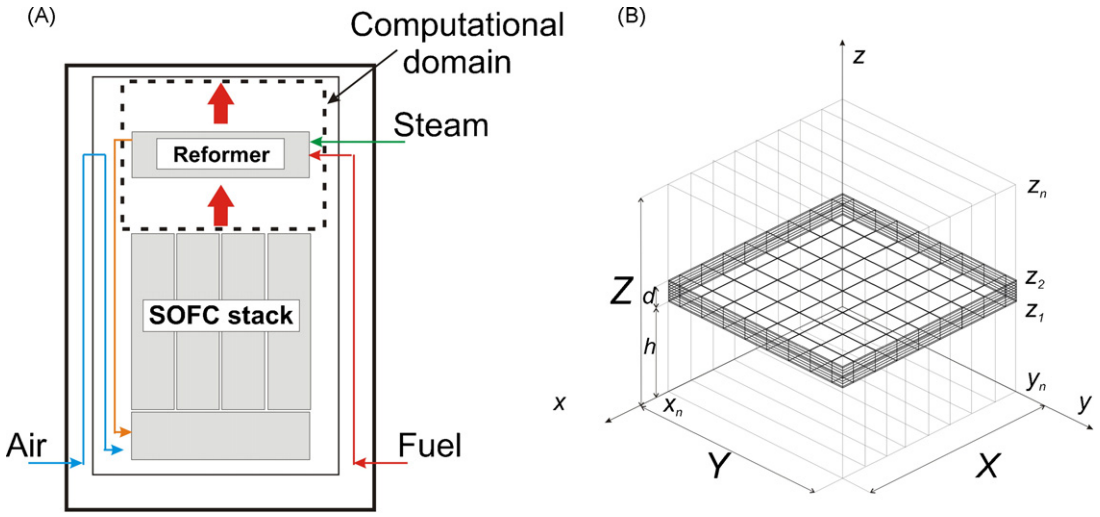

Fig. 1. Configuration of the SOFC system (A) and the grid used for numerical computation (B).

to be instantly approaching the temperature of the reformer. The analysis of heat transfer between the reformer and SOFC chamber illustrates that more than 98% of energy is transported by radiation, less than 1.9% of energy is transported by convection and less than 0.02% of energy is transported by conduction.

2.1. Radiative heat transfer model

The geometry of the radiative heat transfer model to be considered is shown schematically in Fig. 1b. The governing equations to be solved are energy balances. Assuming the absence of free and forced convection inside the closed surface system, the rigorous formulation of energy balances on various surfaces yields an integral equation which can be written as

$$\int_{A_i} \mathrm{d}A_i \int_{A_j} \int_{\lambda=0}^{\infty} \left[\frac{W_{\lambda j} \cos\theta_{ij} \cos\theta_{ji} \varepsilon_{\lambda j}}{\pi r_{ij}^2} \right] \mathrm{d}A_j \mathrm{d}\lambda - \int_{A_i} \mathrm{d}A_i \int_{\lambda=0}^{\infty} \varepsilon_{\lambda i} E_{\lambda i} \mathrm{d}\lambda + \int_{A_i} q_i \mathrm{d}A_i = 0 \quad (1)$$

where $\mathrm{d}A_i$ is the area of the free surface element, θ_{ij} is the angle between r_{ij} and the normal to $\mathrm{d}A_i$, W, λ, E, ε and q are the leaving flux density (radiosity), wavelength, black-body flux density, emissivity and heat flux, respectively.

The energy balance on the surface A_i (Eq. (1)) contains various terms: absorption of incidental radiation from all other surface elements, emission by surface A_i and the heat flux extracted through surface A_i. Considering an enclosure of any shape with walls varying in temperature in any manner and assuming that the walls are grey, Eq. (1), based on the Hottel zone method [16], is written as

$$\sum_{j=1}^{n} \overline{S_j S_i} E_j - A_i \varepsilon_i E_i + A_i q_i = 0, \quad i = 1, \ldots, m \quad (2)$$

where $E_i = \sigma T^4$, E_i is the black-body flux density, T is temperature, σ is the Stefan–Boltzmann constant ($\sigma = 5.6667 \times 10^{-8}\,\mathrm{W\,m^{-2}\,K^{-4}}$), ε_i is the emissivity of the ith surface, and $\overline{S_j S_i}$ is the total interchange area between surface zones s_i and s_j.

The radiosity W_j can be expressed as

$$W_j = \varepsilon_j E_j + \rho_j H_j$$

where H_j and ρ_j are incident radiant flux density and reflectance, respectively.

The value of the total interchange area $\overline{S_j S_i}$ between surface zone s_i and surface zone s_j is determined by

$$\overline{S_j S_i} = \left(\frac{A_j \varepsilon_j}{\rho_j} \right) ({}_{si}W_j - \delta_{ij} \varepsilon_i) \quad (3)$$

where

$${}_{si}W_j = \left(\frac{A_i \varepsilon_i}{\rho_i} \right) \left(-\frac{D_{ij}}{D} \right)$$

D represents the determinant of the matrix $[\overline{s_i s_j} - \delta_{ij}(A_i/\rho_i)]$, δ_{ij} is the Kronecker delta and D_{ij} is the cofactor of matrix $[\overline{s_i s_j} - \delta_{ij}(A_i/\rho_i)]$.

The direct interchange area $\overline{s_i s_j}$ or the view factor φ_{ij}, between the surface zones s_i and s_j may be evaluated by integration of the equation

$$\overline{s_i s_j} = \int_{A_i} \int_{A_j} [(\cos\theta_{ij} \cos\theta_{ji})/(\pi r_{ij}^2)] \mathrm{d}A_i \mathrm{d}A_j \quad (4)$$

where $\overline{s_i s_j} = A_i \varphi_{ij}$, φ_{ij} is the view factor, and A_i the area of the ith surface.

For a closed system of surfaces containing transparent gas, the following relation should be satisfied:

$$\overline{s_i s_j} = \overline{s_j s_i} \quad \text{or} \quad A_i \varphi_{ij} = A_j \varphi_{ji}$$

and

$$\sum_j \overline{s_i s_j} = A_i$$

$$\sum_j \overline{S_i S_j} = \varepsilon_i A_i$$

2.2. Mathematical model of internal indirect reforming SOFC system

2.2.1. Heat transfer model inside the reformer

The fuel is continuously supplied to a reformer to maintain appropriate operating conditions for the fuel cells stack. The most basic governing equations to be solved by numerical modelling are for the velocity, temperature and concentration fields in the internal reformer. They are different among two kinds of areas: solid area and porous area.

For the solid part (the wall of the fuel reformer) the governing equation to be solved is considered to be the following three-dimensional heat conduction equation without internal heat generation:

$$\frac{\partial T}{\partial x}\left(\lambda_{\mathrm{w}}\frac{\partial T}{\partial x}\right)+\frac{\partial T}{\partial y}\left(\lambda_{\mathrm{w}}\frac{\partial T}{\partial y}\right)+\frac{\partial T}{\partial z}\left(\lambda_{\mathrm{w}}\frac{\partial T}{\partial z}\right)=0 \tag{5}$$

where λ_{w} [$\mathrm{W\,m^{-1}\,K^{-1}}$] is the conductivity of the solid wall of the reformer.

The heat flux in Eq. (2) can be expressed as

$$q_i=\frac{T_i-T_{i-1}}{R_i} \tag{6}$$

where $R_i=d_i/\lambda_{\mathrm{w}}$, T_i is the temperature of the ith surface and d is the thickness of the reformer wall.

The microstructure of porous media is not to be considered directly in the present model therefore for the porous area, the governing equations derived by the volume-averaging method are applied. In the adopted method physical values are locally averaged for a representative elementary volume [17]. The representative volume is sufficiently larger than the scale of the fine structure of the porous medium and is sufficiently smaller than the scale of the porous body itself [15]. The heat transfer process inside the reformer porous media is described by continuity, momentum, energy and mass transfer equations. Consequently the following transport equations of the averaged physical values for laminar flows apply

$$\frac{\partial\rho_0 U_x}{\partial x}+\frac{\partial\rho_0 U_y}{\partial y}+\frac{\partial\rho_0 U_z}{\partial z}=0 \tag{7}$$

$$\begin{aligned}&\frac{\rho_0}{\varepsilon_0^2}\left(U_x\frac{\partial U_x}{\partial x}+U_y\frac{\partial U_x}{\partial y}+U_z\frac{\partial U_x}{\partial z}\right)\\&=-\frac{\partial P}{\partial x}+\frac{1}{\varepsilon_0}\left[\frac{\partial}{\partial x}\left(\mu\frac{\partial U_x}{\partial x}\right)+\frac{\partial}{\partial y}\left(\mu\frac{\partial U_x}{\partial y}\right)\right.\\&\left.+\frac{\partial}{\partial z}\left(\mu\frac{\partial U_x}{\partial z}\right)\right]-\frac{\mu}{K}U_x-\frac{\rho_0 f}{\sqrt{K}}U_x\sqrt{U_x^2+U_y^2+U_z^2}\end{aligned} \tag{8a}$$

$$\begin{aligned}&\frac{\rho_0}{\varepsilon_0^2}\left(U_x\frac{\partial U_y}{\partial x}+U_y\frac{\partial U_y}{\partial y}+U_z\frac{\partial U_y}{\partial z}\right)\\&=-\frac{\partial P}{\partial y}+\frac{1}{\varepsilon_0}\left[\frac{\partial}{\partial x}\left(\mu\frac{\partial U_y}{\partial x}\right)+\frac{\partial}{\partial y}\left(\mu\frac{\partial U_y}{\partial y}\right)\right.\\&\left.+\frac{\partial}{\partial z}\left(\mu\frac{\partial U_y}{\partial z}\right)\right]-\frac{\mu}{K}U_y-\frac{\rho_0 f}{\sqrt{K}}U_y\sqrt{U_x^2+U_y^2+U_z^2}\end{aligned} \tag{8b}$$

$$\begin{aligned}&\frac{\rho_0}{\varepsilon_0^2}\left(U_x\frac{\partial U_z}{\partial x}+U_y\frac{\partial U_z}{\partial y}+U_z\frac{\partial U_z}{\partial z}\right)\\&=-\frac{\partial P}{\partial z}+\frac{1}{\varepsilon_0}\left[\frac{\partial}{\partial x}\left(\mu\frac{\partial U_z}{\partial x}\right)+\frac{\partial}{\partial y}\left(\mu\frac{\partial U_z}{\partial y}\right)\right.\\&\left.+\frac{\partial}{\partial z}\left(\mu\frac{\partial U_z}{\partial z}\right)\right]-\frac{\mu}{K}U_z-\frac{\rho_0 f}{\sqrt{K}}U_z\sqrt{U_x^2+U_y^2+U_z^2}\end{aligned} \tag{8c}$$

$$\begin{aligned}&\rho_0 C_{\mathrm{p}}\left(U_x\frac{\partial T}{\partial x}+U_y\frac{\partial T}{\partial y}+U_z\frac{\partial T}{\partial z}\right)\\&=\frac{\partial}{\partial x}\left(\lambda_{\mathrm{eff}}\frac{\partial T}{\partial x}\right)+\frac{\partial}{\partial y}\left(\lambda_{\mathrm{eff}}\frac{\partial T}{\partial y}\right)+\frac{\partial}{\partial z}\left(\lambda_{\mathrm{eff}}\frac{\partial T}{\partial z}\right)+Q\end{aligned} \tag{9}$$

$$\begin{aligned}&U_x\frac{\partial\rho_0 Y_j}{\partial x}+U_y\frac{\partial\rho_0 Y_j}{\partial y}+U_z\frac{\partial\rho_0 Y_j}{\partial z}\\&=\frac{\partial}{\partial x}\left(\rho_0 D_{jm,\mathrm{eff}}\frac{\partial Y_j}{\partial x}\right)+\frac{\partial}{\partial y}\left(\rho_0 D_{jm,\mathrm{eff}}\frac{\partial Y_j}{\partial y}\right)\\&+\frac{\partial}{\partial z}\left(\rho_0 D_{jm,\mathrm{eff}}\frac{\partial Y_j}{\partial z}\right)+S_j\end{aligned} \tag{10}$$

The physical values in the above equations represent the local phase average of the gas control volume, U_x, U_y and U_z are the gas phase average x-, y- and z-components of the local gas velocity. T is the local average temperature over both the gas and solid phases. The $\varepsilon_0=0.9$ and $K=1.0\times10^{-7}\,\mathrm{m^2}$ are the porosity and permeability of the porous medium, respectively. The $f=0.0088$ is the inertia coefficient which depends on the Reynolds number and the microstructure of the porous medium [18]. $\lambda_{\mathrm{eff}}=\{\varepsilon_0\lambda_{\mathrm{f}}+(1-\varepsilon_0)\lambda_{\mathrm{s}}\}$ [$\mathrm{W\,m^{-1}\,K^{-1}}$] is the effective thermal conductivity, where λ_{f} represents fluid thermal conductivity and $\lambda_{\mathrm{s}}=10.0\,\mathrm{W\,m^{-1}\,K^{-1}}$ is the solid phase thermal conductivity [15]. $D_{jm,\mathrm{eff}}=(1-\sqrt{1-\varepsilon_0})D_{jm}$ [$\mathrm{m^2\,s^{-1}}$] is the effective mass diffusivity of species j. Y_j is the mass fraction of chemical species j and D_{jm} is the mass diffusivity of species j in the multi-component mixture of gases, respectively. All gas components are treated as ideal gases in the calculation of density. In the calculations of the thermal field, temperature is adapted as a variable to solve but the thermodynamic properties (specific heat at constant pressure, enthalpy, Gibb's free energy) and transport properties (viscosity, heat conductivity) are treated as functions of temperature. Their local values are calculated at local temperature by taking data from the liquids and gases properties tables [19]. Properties of mixtures are evaluated with mixing laws [20].

2.2.2. Mathematical model for fuel reforming process

The methane/steam reforming process is widely known as a conventional process for producing hydrogen [21,22] and it proceeds on catalysts such as nickel–alumina. In the methane with steam reforming process, the dominant reactions are the following two [14]:

- fuel reforming reaction

$$CH_4 + H_2O = 3H_2 + CO, \quad \Delta H^0_{1300} = 227.5\,\mathrm{kJ\,mol^{-1}} \tag{11}$$

- shift reaction

$$CO + H_2O = H_2 + CO_2, \quad \Delta H^0_{1300} = -31.8\,\mathrm{kJ\,mol^{-1}} \tag{12}$$

The fuel reforming reaction described by Eq. (11) is a slow and highly endothermic reaction; therefore a supply of thermal energy is needed for the reforming reaction. Also, how methane is reformed inside the reformer is dependent on the local conditions, including not only temperature but also partial pressure of each chemical species as well as the density of the catalysts or catalysts' active area [15]. The water–gas shift reaction described by Eq. (12) is a fast and weak exothermic reaction and can be assumed to be in equilibrium at the reforming temperature [14].

The reaction rates of the two above reactions (Eqs. (11) and (12)) R_{st} and R_{sh} are locally calculated as follows:

$$R_{st} = A_{cat} k_{CH_4} p_{CH_4} \exp\left(-\frac{E_{CH_4}}{RT}\right) \tag{13}$$

$$R_{sh} = K^+_{sh} p_{CO} p_{H_2O} - K^-_{sh} p_{H_2} p_{CO_2} \tag{14}$$

Eq. (13) is based on the Achenbach model [12] where A_{cat} is the catalysts active area of steam reforming reaction in a control volume of reformer [$m^2\,m^{-3}$], T [K] is the fuel conversion temperature, $R_u = 8.314472\,\mathrm{J\,mol^{-1}\,K^{-1}}$ is the universal gas constant, $E_{CH_4} = 8.2 \times 10^4\,\mathrm{J\,mol^{-1}}$ is the activation energy of the fuel reforming reaction [11], $k_{CH_4} = 4274 \times 10^{-5}\,\mathrm{mol\,m^{-2}\,Pa^{-1}\,s^{-1}}$ is the pre-exponential factor [11] and p_{CH_4} is the partial pressure of methane [Pa]. The active area A_{cat} is an important parameter in a sense that control of its distribution can be used as a means to change the distribution pattern of the reformer temperature.

K^+_{sh} and K^-_{sh} denote the rate constants of forward and backward water–gas shift reactions and the value of R_{sh} is determined by a method described by Lehnert et al. [23]. The water shift reaction determined by Eq. (12) reaches equilibrium rapidly; therefore CO_2, H_2, CO and H_2O have to satisfy the equilibrium equation. Chemical equilibrium is represented by the equilibrium constant, which is a function of temperature and is equal to the ratio between the reactants' and products' partial pressures.

$$K_{sh} = \frac{K^+_{sh}}{K^-_{sh}} = \frac{p_{CO_2} p_{H_2}}{p_{CO} p_{H_2O}} = \exp\left(-\frac{\Delta G^\circ_{sh}}{RT}\right) \tag{15}$$

where ΔG°_{sh} is the change of standard Gibbs free energy of shift reaction.

This equilibrium constant given by Eq. (15) is introduced into Eq. (14) to calculate the rate of the shift reaction.

The mass production or consumption rate of each chemical species by the fuel reforming reaction (Eq. (11)) and shift reaction (Eq. (12)) is also calculated as follows:

$$\dot{S}_{H_2} = 3R_{st}M_{H_2} + R_{sh}M_{H_2} \tag{16a}$$

$$\dot{S}_{CO} = R_{st}M_{CO} - R_{sh}M_{CO} \tag{16b}$$

$$\dot{S}_{CO_2} = R_{sh}M_{CO_2} \tag{16c}$$

$$\dot{S}_{CH_4} = -R_{st}M_{CH_4} \tag{16d}$$

$$\dot{S}_{H_2O} = -R_{st}M_{H_2O} - R_{sh}M_{H_2O} \tag{16e}$$

The value of mass production or consumption rate for each chemical species is introduced into the species mass transfer (Eq. (10)) as a part of its source term.

The thermodynamic heat generation rate by the reforming reactions (Eqs. (11) and (12)) is calculated based on the reaction rates, as follows:

$$Q_{st} = -\Delta H_{st} R_{st} \tag{17a}$$

$$Q_{sh} = -\Delta H_{sh} R_{sh} \tag{17b}$$

where ΔH_{st} and ΔH_{sh} are the enthalpy change accompanied with each reaction.

The heat conduction and convection equations were solved numerically by finite volume method [24]. The resulting radiation–conduction–convection conjugate heat transfer problems were subsequently numerically solved by Gauss–Seidel [25] and Newton–Raphson methods [16].

3. Numerical results

Numerical simulation is a potential tool for investigating the flow, thermal and chemical species concentration fields in the module chamber of an internal indirect reforming-type SOFC process. In practice this process involves radiation between surfaces, heat conduction in the solid area, forced convection in the porous one and the methane/steam reforming process proceeds on the catalysts. However, applying numerical simulation enables the artificial exclusion of the forced convection effect in the porous area or the methane/steam reforming process effects in order to investigate transport phenomena in detail. Therefore, the calculations are presented for two different problems: the radiation–conduction conjugate heat transfer problem without the methane/steam reforming process and the radiation–conduction–convection conjugate heat transfer problem with the methane/steam reforming process. Numerical computations for both problems were performed for two different thermal boundary tests (Tests I and II). Test I: the first kind of thermal boundary was considered, i.e. the temperature distribution of the SOFC stack and the temperature of other elements in the SOFC module were assumed (see Fig. 1). Test II: the second kind of thermal boundary was considered, i.e. constant heat flux from the SOFC stack and constant ambient temperature were assumed. Numerical calculations were carried out for different positions of the reformer in the module chamber and emissivity of the surfaces (i.e. different emissivity of the reformer, cell and other elements in the SOFC module). Table 1 summarized the thermal boundary conditions applied in computations.

Table 1
Thermal boundary condition

	Test Ia	Test IIa	Test Ib	Test Ic	Test IIb
Temperature of the bottom	1123 K		1123 K	1123 K	
Temperature of the top wall	923 K		1123 K	923 K	
Temperature of the side walls	773 K		1123 K	773 K	
Heat flux from the SOFC stack		6 kW m^{-2}			10 kW m^{-2}
Thermal conductivity of the side walls		1 W m^{-1} K^{-1}			0.5 W m^{-1} K^{-1}
'Ambient' temperature		500 K			500 K

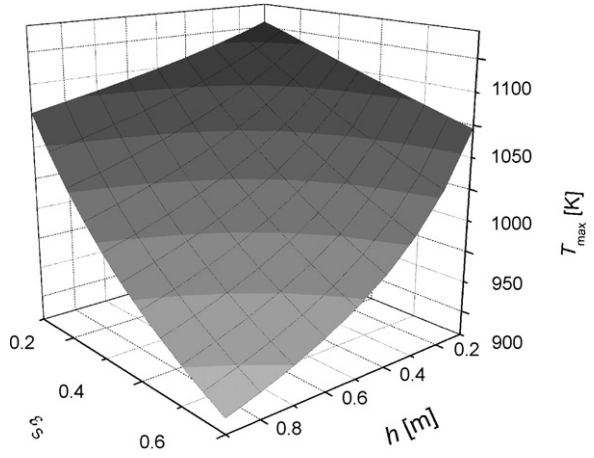

Fig. 2. The maximum value of temperature inside the reformer as a function of the distance between the fuel reformer and SOFC stack and side walls emissivity, for the first problem and thermal boundary Test Ia: $T_B(x, y, 0) = 1123$ K, $T_T(x, y, z_n) = 923$ K, $T_S = 773$ K, thermal conductivity of the reformer, $\lambda_R = 1.0$ W m^{-1} K^{-1} and the emissivity of the horizontal walls was $\varepsilon = 0.5$.

The examples of numerical results for the first problem are shown in Figs. 2 and 3. Fig. 2 shows examples of the results of numerical computations for thermal boundary Test Ia. The temperatures of the bottom, top and side walls were assumed to be constant; the temperature of the bottom is $T_B(x, y, 0) = 1123$ K, the temperature of the top wall is $T_T(x, y, z_n) = 923$ K, and the temperature of the side walls is $T_S = 773$ K. Fig. 2 presents the maximum temperature inside the reformer as a function of the distance between the fuel reformer and SOFC stack and the side wall emissivity. The emissivity of the horizontal walls was $\varepsilon = 0.5$, the thermal conductivity of the reformer was $\lambda_R = 1.0$ W m^{-1} K^{-1}. Fig. 3 shows examples of the results of numerical computations for thermal boundary Test IIa. The heat flux from the SOFC stack has the value $q = 6000.0$ W m^{-2}, and 'ambient' temperature was $T_0 = 500$ K; the thermal conductivity of the side walls λ_S equals 1.0 W m^{-1} K^{-1} and thermal conductivity of the reformer λ_R equals 0.5 W m^{-1} K^{-1}. Fig. 3 presents the maximum value of temperature inside the reformer as a function of the distance between the fuel reformer and SOFC stack and side walls emissivity. As is evident in Figs. 2 and 3, the temperature inside the reformer is strongly affected by both the position of the module chamber and by the walls' emissivity. As the value of h decreases (i.e. the distance between the reformer and SOFC stack decreases) the temperature inside the reformer increases. The calculated temperature distributions inside the reformer show that the value of the temperature depends on the walls' emissivity (i.e. the emissivity of the bottom reformer wall, emissivity of the SOFC stack and the side walls in the SOFC module). Analyses of numerical results have proved to be interesting. For example, when the emissivity of the side walls decreases the temperature inside the reformer increases. However, when the emissivity value of the bottom reformer wall and/or the emissivity of the SOFC stack increase then the temperature inside the reformer increases as well [26].

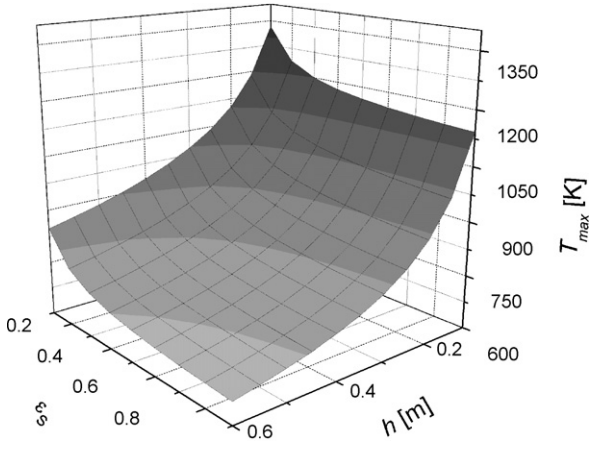

Fig. 3. The maximum value of temperature inside the reformer as a function of the distance between the fuel reformer and SOFC stack and side wall emissivity, for the first problem and thermal boundary Test IIa: $q = 6000.0$ W m^{-2}, $T_0 = 500$ K, thermal conductivity of the reformer, $\lambda_R = 0.5$ W m^{-1} K^{-1} thermal conductivity of the side walls $\lambda_S = 1.0$ W m^{-1} K^{-1} and the emissivity of the horizontal walls was $\varepsilon = 0.5$.

The examples of numerical results for the second problem are shown in Figs. 4–9. Figs. 4 and 5 show examples of the results of numerical computations for thermal boundary Test Ib. The temperature of the bottom, top and side walls was assumed to be constant; $T_B(x, y, 0) = T_T(x, y, z_n) = T_S = 1123$ K. The inlet molar flow rate of methane has the value $n_{CH_4} = 0.2 \times 10^{-4}$ kmol s^{-1}, the steam-to-carbon ratio equals 2.5, pressure inside the reformer chamber was $P = 1.01 \times 10^5$ Pa, the catalysts active area has the value $A_{cat} = 10$ m^2, the volume of reformer equals 0.1 m^3, the distance between stack and fuel reformer was $h = 0.35$ m, and the emissivity of all surfaces in the system ε equals 0.5. Fig. 4 presents the distribution of temperature and the distribution of methane inside the reformer in the longitudinal direction of the fuel reformer. The average temperature and change of the molar flow rate of methane in the longitudinal direction of the fuel reformer are illustrated by Fig. 5. As is evident in Figs. 4 and 5,

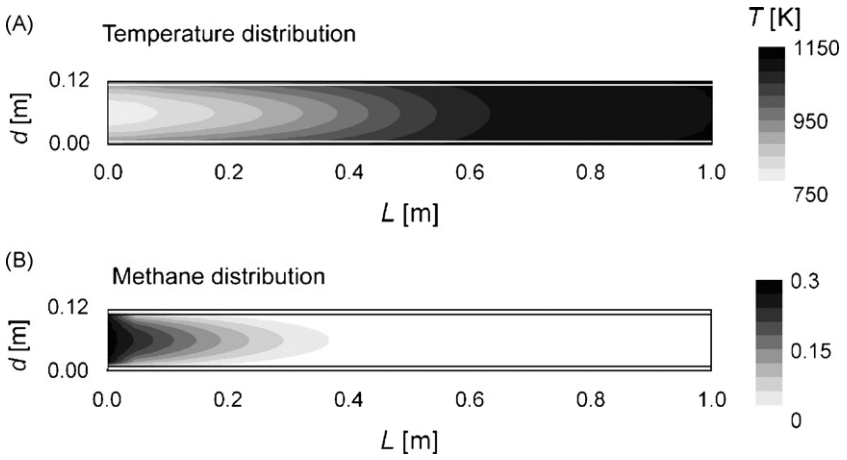

Fig. 4. Temperature distribution (A) and CH_4 distribution (B) in the longitudinal direction of the fuel reformer (thermal boundary Test Ib).

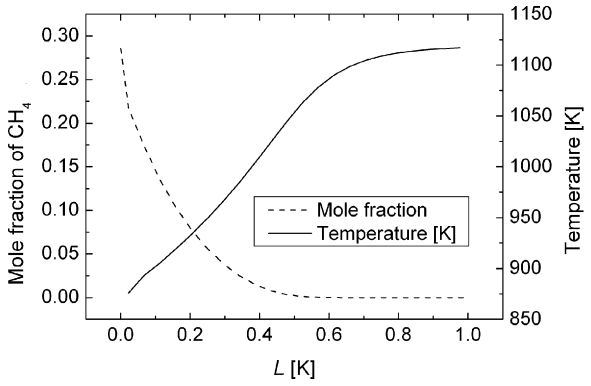

Fig. 5. Average temperature and change of methane molar flow rate in the longitudinal direction of the fuel reformer (thermal boundary Test Ib).

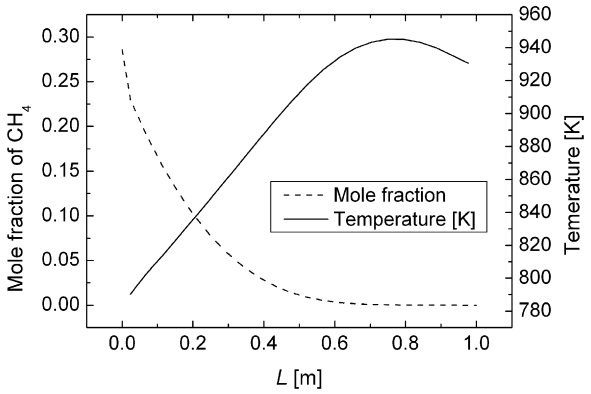

Fig. 7. Average temperature and change of methane molar flow rate in the longitudinal direction of the fuel reformer (thermal boundary Test Ic).

the distribution of temperature inside the reformer is not uniform, and when the molar flow rate of methane decreases the temperature inside the reformer increases (Figs. 4 and 5). The reforming reaction is strongly endothermic, therefore the temperature decreases at the reformer inlet.

Figs. 6 and 7 show the results of numerical computations for different configurations of thermal boundary Test Ic. The temperature of the bottom, top and side walls was assumed to be constant; the temperature of the bottom is $T_B(x, y, 0) = 1123$ K, the temperature of top wall is $T_T(x, y, z_n) = 973$ K, and the temperature of the side walls is $T_S = 773$ K. The inlet molar flow rate of methane has the value $n_{CH_4} = 0.1 \times 10^{-4}$ kmol s^{-1}, the steam-to-carbon ratio equals 2.5, pressure inside reformer chamber was $P = 1.01 \times 10^5$ Pa, the catalysts active area has the value $A_{cat} = 10$ m^2, the reformer volume equals 0.1 m^{-3}, the distance

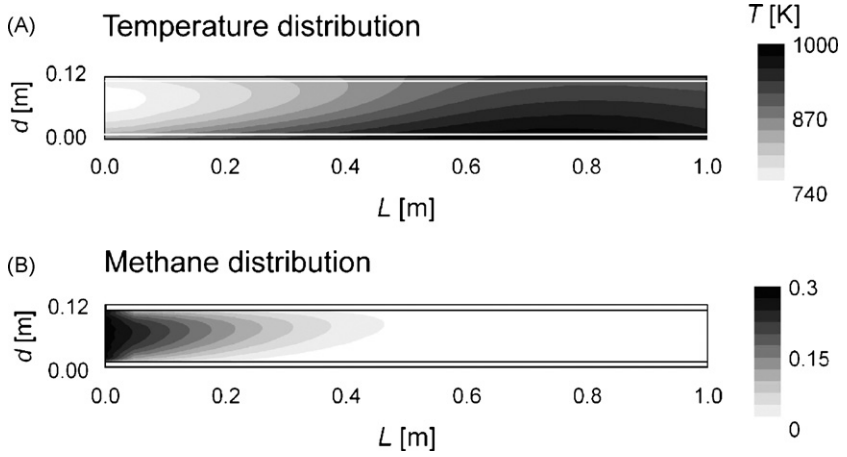

Fig. 6. Temperature distribution (A) and CH_4 distribution (B) in the longitudinal direction of the fuel reformer (thermal boundary Test Ic).

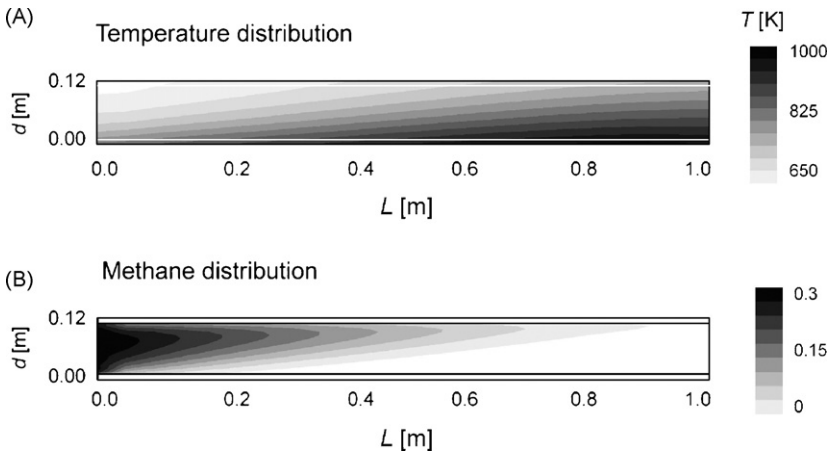

Fig. 8. Temperature distribution (A) and CH_4 distribution (B) in the longitudinal direction of the fuel reformer (thermal boundary Test IIb).

between stack and fuel reformer was $h = 0.1$ m, and the emissivity of all surface in the system is ε equals 0.5. Fig. 6 presents the distribution of temperature and the distribution of methane inside the reformer in the longitudinal direction of the fuel reformer. The average temperature and change of the molar flow rate of methane in the longitudinal direction of the fuel reformer are presented in Fig. 7. As is evident in Figs. 4–7, the temperature inside the reformer is strongly affected by the position of the module chamber and temperature distribution of side walls. As the temperatures of the side walls decrease, so too does the average temperature inside the reformer.

Figs. 8 and 9 exemplify the results of numerical computations for thermal boundary Test IIb. The heat flux from the SOFC stack has the value $q = 10{,}000\ \mathrm{W\,m^{-2}}$ and 'ambient' temperature was $T_0 = 500$ K; the thermal conductivity of the side walls λ_S equals $0.5\ \mathrm{W\,m^{-1}\,K^{-1}}$ and the emissivity of all surfaces in the system was $\varepsilon = 0.5$. The inlet molar flow rate of methane has the value $n_{CH_4} = 0.1 \times 10^{-4}\ \mathrm{kmol\,s^{-1}}$, the steam-to-carbon ratio equals 2.5, the distance between stack and fuel reformer was $h = 0.1$ m, the pressure inside reformer chamber was $P = 1.01 \times 10^5$ Pa, the catalysts active area has the value $A_{cat} = 10\ \mathrm{m^2}$, the volume of reformer equals $0.1\ \mathrm{m^{-3}}$. Fig. 8 presents the distribution of temperature and the distribution of methane inside the reformer in the longitudinal direction of fuel reformer. The average temperature and change of the molar flow rate of methane in the longitudinal direction of fuel reformer are illustrated by Fig. 9. Analyses of the numerical results proved interesting. For example, the distribution of temperature inside the reformer is strongly effected by the kind of thermal boundary adapted in numerical tests.

In the most existing literature for SOFC model the radiation is often simply described by the two face-to-face planes. An example of comparison of numerical results obtained by model presented in this paper and simplified model 'two face-to-face planes' is shown in Fig. 10. In the numerical calculations presented in Fig. 10, the heat flux from the SOFC stack has the value $q = 6000.0\ \mathrm{W\,m^{-2}}$, and 'ambient' temperature was $T_0 = 500$ K; the thermal conductivity of the top wall λ_T equals $1.0\ \mathrm{W\,m^{-1}\,K^{-1}}$ and thermal conductivity of the reformer λ_R equals $2.0\ \mathrm{W\,m^{-1}\,K^{-1}}$, side walls were insulated. As is evident in Fig. 10 the calculated temperature distribution depends on the numerical modelling. The temperature distribution obtained by simplified model is much lower and is not 'realistic' (i.e. we cannot see maximum value of temperature in central part of the reformer). Analyses of the numerical results obtained by these two models have proved the necessity of the complex calculations.

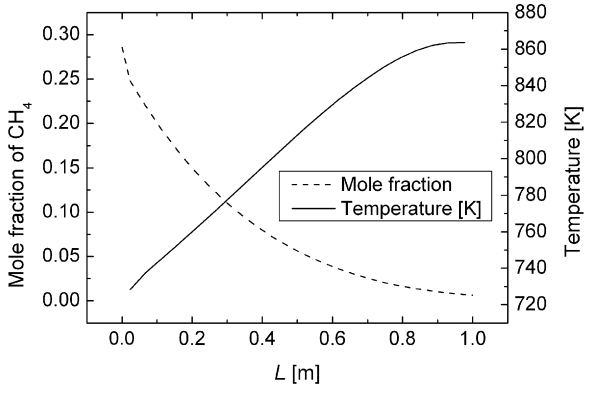

Fig. 9. Average temperature and change of methane molar flow rate in the longitudinal direction of the fuel reformer (thermal boundary Test IIb).

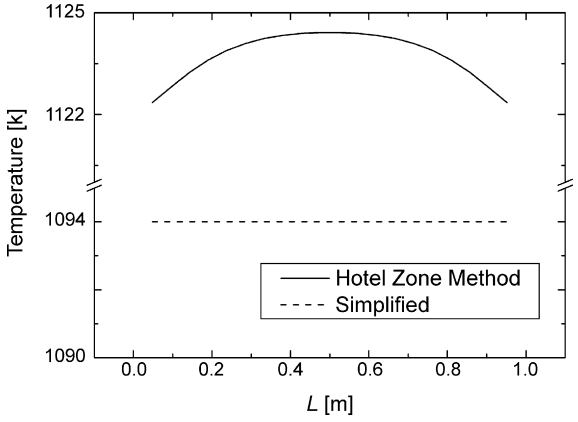

Fig. 10. Temperature distribution at the bottom wall of reformer (comparison of numerical results obtained by present model and by the face-to-face planes model).

4. Conclusions

The present paper describes the numerical modelling of the radiative heat transfer process in the module chamber of an internal indirect reforming-type SOFC. As in any high-temperature system, radiative heat transfer effects are significant and need to be accounted for to accurately predict temperatures in the SOFC module. In this article, governing equations for radiative heat transfer are described using Hottel's zone method. The steam reforming reaction occurring inside the fuel reformer is described using Achenbach model. The resulting radiation–conduction–convection conjugate heat transfer problems are numerically solved with a combination of the Gauss–Seidel and Newton–Raphson methods. The obtained results indicate that, for the development of effective indirect internal reforming, the position of the reformer in the module chamber and emissivity of the surfaces of the reformer, cell and other elements in the SOFC module all play a key role. As the distance between the reformer and SOFC stack decreases the temperature inside the reformer increases. When the emissivity of the side walls decreases the temperature inside the reformer increases. However, when the emissivity value of the bottom reformer wall and/or the emissivity of the SOFC stack increases then the temperature inside the reformer increases as well.

Acknowledgements

This work was supported by the European Commission (project Dev-BIOSOFC, FP6-042436, MTKD-CT-2006-042436).

References

[1] O. Yamamoto, Electrochem. Acta 45 (2000) 2423.
[2] P. Aguiar, D. Chadwick, L. Kershenbaum, Chem. Eng. Sci. 57 (2002) 1665.
[3] K. Eguchi, in: K. Suzuki (Ed.), International Workshop on Fuel Cell and Fuel Cell Hybrid Systems, Energy Flow Research Center, Research Organization for Advanced Engineering, Tokyo, 2004, p. 13.
[4] T.Q. Minh, T. Takahashi, Science and Technology of Ceramic Fuel Cells, Elsevier, New York, 1995, p. 1.
[5] P.-W. Li, K. Suzuki, J. Electrochem. Soc. 151 (2004) A548.
[6] T.W. Song, J.L. Sohn, J.H. Kim, T.S. Kim, S.T. Ro, K. Suzuki, J. Power Sources 142 (2005) 30.
[7] K.P. Recknagle, R.E. Wiliford, L.A. Chick, M.A. Rector, M.A. Khaleel, J. Power Sources 113 (2003) 109.
[8] S. Murthy, A.G. Fedorov, J. Power Sources 124 (2003) 453.
[9] H. Yakabe, T. Ogiwara, I. Yasuda, M. Hishunuma, J. Power Sources 102 (2001) 144.
[10] D.L. Damm, A.G. Fedorov, J. Power Sources 143 (2005) 158.
[11] E. Achenbach, E. Riensche, J. Power Sources 52 (1994) 283–288.
[12] E. Achenbach, J. Power Sources 49 (1994) 333–348.
[13] R. Odegard, E. Jornsen, H. Karoliussen, in: M. Dokiya, O. Yamoto, H. Tagawa, S.C. Singhal (Eds.), Proceedings of the Fourth International Symposium on Solid Oxide Fuel Cells, Penninyton, NJ, 1995, pp. 810–819.
[14] S. Nagata, A. Momma, T. Kato, Y. Kasuga, J. Power Sources 101 (2001) 60–71.
[15] K. Suzuki, H. Iwai, T. Nishino, in: B. Suden, M. Faghir (Eds.), Transport Phenomena in Fuel Cells, WIT Press, Lund, 2005, p. 95.
[16] H.C. Hottel, A.F. Sarofim, Radiative Transfer, McGraw Hill, New York, 1968, p. 100.
[17] R.G. Carbonell, S. Whitaker, in: J. Bear, M.Y. Corapciglu (Eds.), Fundamentals of Transport Phenomena in Porous Media, Martinus Nijhoff Publishers, Dordrecht, 1984, pp. 123–198.
[18] K. Vafai, C.L. Tien, Int. J. Heat Mass Transfer 24 (1981) 195–203.
[19] B.E. Poling, J.M. Prausnitz, J.P. O'Connell, The Properties of the Gases and Liquids, 5th edition, McGrawHill, New York, 2000, p. 10.30.
[20] C.R. Wilke, Chem. Eng. Prog. 46 (2000) 95–104.
[21] J. Xu, G.F. Froment, AIChE J. 35 (1989) 88–96.
[22] J. Xu, G.F. Froment, AIChE J. 35 (1989) 97–103.
[23] W. Lehnert, J. Meusinger, F. Thom, J. Power Sources 87 (2000) 57–63.
[24] S.V. Patankar, Numerical Heat Transfer and Fluid Flow, Hemisphere, New York, 1980, p. 10.
[25] J.H. Ferziger, M. Perić, Computational Methods for Fluid Dynamics, Springer, Berlin, 1996, p. 10.
[26] G. Brus, J.S. Szmyd, Proceedings of the 10th International Symposium on Solid Oxide Fuel Cells, Nara, 2007, pp. 2013–2020.
[27] Japanese Patents 2005-183375 A.